Clinical Feasibility of Coherence-Based Beamforming to Distinguish Solid from Fluid Hypoechoic Breast Masses

Alycen Wiacek*, Eniola Falomo†, Kelly Myers†, Ole Marius Hoel Rindal‡, Kelly Fabrega-Foster†, Susan Harvey† and Muyinatu A. Lediju Bell*§¶

*Department of Electrical and Computer Engineering, Johns Hopkins University, Baltimore, MD
†Department of Radiology and Radiological Science, Johns Hopkins Medicine, Baltimore, MD
‡Department of Informatics, University of Oslo, Oslo, Norway
§Department of Biomedical Engineering, Johns Hopkins University, Baltimore, MD
¶Department of Computer Science, Johns Hopkins University, Baltimore, MD

***Abstract*—Ultrasound imaging is often used in conjunction with mammography, particularly for patients with dense breast tissue, which causes an increased amount of acoustic clutter, obscuring lesions of interest, and contributing to the false positive rate of breast ultrasound. Coherence-based imaging methods, such as short-lag spatial coherence (SLSC) and robust short-lag spatial coherence (R-SLSC), display the coherence of backscattered ultrasound signals instead of their amplitude or brightness information, which offers opportunities to reduce acoustic clutter. This paper focuses on SLSC and R-SLSC beamforming applied to three *in vivo* masses in the female breast: (1) cyst, (2) fibroadenoma, and (3) ductal carcinoma in situ (DCIS). Contrast is improved by up to 7.8 dB with SLSC imaging and 4.86 dB with R-SLSC imaging in fluid-filled regions. However, contrast is degraded in coherence-based images of solid hypoechoic lesions because coherence is displayed in these regions with pathologically determined solid content. This interesting finding indicates the potential of coherence-based imaging to assist with the differentiation between solid and fluid-filled hypoechoic breast masses. Examples of duplex mode B-mode and R-SLSC images are shown to convey clinical potential.**

I. Introduction

Breast cancer is the leading cause of cancer death for women in the world; over 600,000 women are predicted to die from the disease in 2018 [1]. Breast ultrasound is widely used as a diagnostic supplement to mammography and has been shown to detect additional cancers previously undetected with mammography [2]. Ultrasound imaging is particularly beneficial in patients with dense breast tissue, where mammographic sensitivity is significantly deteriorated [3]. In the ACRIN 6666 trial specifically, more false positives were seen in ultrasound with increasing breast density (10% false positives with $\leq$25% density steadily increasing to 14.4% false positives with breast density $>$80%) [4]. This trend is indicative of the acoustic interactions between dense breast tissue that cause phase aberrations and acoustic clutter [5], [6]. Advanced beamforming techniques aimed at reducing clutter in ultrasound images or measuring additional properties of tissue are particularly well suited for clinical application [7], [8]. These techniques have potential to reduce the number of false positives obtained with breast ultrasound imaging

In particular, short-lag spatial coherence (SLSC) [9] and robust short-lag spatial coherence (R-SLSC) [10] are two advanced beamforming techniques that have potential to reduce acoustic clutter and improve breast ultrasound image quality. Since its introduction as a clutter reduction technique, SLSC has been applied to a variety of *in vivo* tissue types including thyroid [9], cardiac [11], fetal [12], [13], and liver [14]. Similarly, R-SLSC has been demonstrated with *in vivo* liver tissue [10]. This technique improves SLSC imaging by denoising the sparse information present at larger lags. Both SLSC and R-SLSC imaging take advantage of the similarity of backscattered pressure waves and are therefore more robust against clutter and other noise sources, making them uniquely suited for breast ultrasound imaging. In this paper, we explore SLSC and R-SLSC beamforming applied to three specific *in vivo* lesions in the human breast: cyst, fibroadenoma, and ductual carcinoma in situ (DCIS).

II. Methods

Three patients were enrolled in our ongoing study after informed consent and approval from the Johns Hopkins Medical Institutions (protocol number IRB00127110). Each patient was scanned using an Alpinion ECUBE12R research ultrasound scanner (Alpinion, Seoul, Korea) connected to an Alpinion L8-17 or Alpinion L3-8 with center frequencies of 12.5MHz and 8MHz, respectively and a sampling frequency of 40MHz. Each lesion was insonified using 256 focused transmissions with a focus as selected by our trained radiologist co-authors.

Contrast, signal-to-noise ratio (SNR), and contrast-to-noise ratio (CNR) were measured and compared across matched B-mode and coherence-based images created with the same channel data according to the following equations:

$$Contrast = 20\log_{10}\left(\frac{S_i}{S_o}\right) \tag{1}$$

$$CNR = \frac{|S_i - S_o|}{\sqrt{\sigma_i^2 + \sigma_o^2}} \tag{2}$$

$$SNR = \frac{S_o}{\sigma_o} \tag{3}$$

where S_i and σ_i are the mean and standard deviation, respectively, within a region of interest (ROI) inside of the target prior to log-compression and S_o and σ_o are the mean and

standard deviation, respectively, of a region of interest outside of the target prior to log-compression.

A. Coherence-Based Beamforming

1) Short-Lag Spatial Coherence (SLSC): SLSC relies on the spatial coherence of backscattered pressure waves received across the ultrasound transducer. After standard receive delays, normalized correlations are calculated between equally spaced elements, or lags, resulting in the normalized spatial correlation:

$$\hat{R}(m) = \frac{1}{N-m} \sum_{i=1}^{N-m} \frac{\sum_{n=n_1}^{n_2} s_i(n) s_{i+m}(n)}{\sqrt{\sum_{n=n_1}^{n_2} s_i^2(n) \sum_{n=n_1}^{n_2} s_{i+m}^2(n)}} \tag{4}$$

where N is the number of elements in the transducer, m is the lag, $s_i(n)$ is a time-delayed, zero-mean signal received at element i from depth n.

The resulting spatial coherence function is then summed up to a specific short-lag value, M, yielding the value of the SLSC pixel.

$$R_{sl} = \int_1^M \hat{R}(m) dm \approx \sum_{m=1}^{M} \hat{R}(m) \tag{5}$$

This process is repeated for each lateral and axial position in the image, typically with an axial correlation kernel of size $k = n_2 - n_1$ [15]. Throughout this work, a kernel of 1.56 times the wavelength associated with the center frequency of the probe was taken.

2) Robust Short-Lag Spatial Coherence (R-SLSC): R-SLSC beamforming improves the original SLSC algorithm by removing outliers in the coherence information. First, each lag image (generated with the SLSC algorithm described above) is vectorized and stacked. This matrix, D, contains the noisy lag images. In order to remove outliers, robust principal component analysis (RPCA) is performed on the noisy D matrix, deriving a solution based on the expression:

$$D = A + E \tag{6}$$

where A is the underlying low-rank matrix, or the denoised coherence information, and E is the sparse error matrix. This expression can be arranged to solve for A using a convex relaxation and the Augmented Lagrange Multiplier (ALM) method implemented by [16]:

$$\begin{aligned} L(A, E, Y, \mu) = ||A||_* + \lambda ||E||_1 + \langle Y, D - A - E \rangle \\ + \frac{\mu}{2} ||D - A - E||_F^2 \end{aligned} \tag{7}$$

where Y is a matrix of Lagrange multipliers, λ is the sparsity penalty parameter that is varied to smooth tissue texture, μ is a positive scalar, $||\cdot||_1$ is the L_1 norm, $||\cdot||_F$ is the Frobenius norm, and $||\cdot||_*$ is the nuclear norm.

After the application of RPCA, the denoised matrix, A is then weighted according to a linearly decreasing weighting scheme, where the lag 1 image is given a weight of 1 down to the lag M image given a weight of $\frac{1}{M}$. After weighting, the vectorization is reversed to form the final R-SLSC image.

B. Sparsity Parameter

There are two parameters of importance in selecting an R-SLSC image for display, namely the short-lag value, M, and the sparsity parameter, λ, as shown in Eq. 7. As demonstrated previously [9], [15], increasing the short-lag value, improves lateral resolution. Varying the sparsity parameter λ, changes the penalty for sparsity within Eq. 7 and therefore affects the level of smoothing applied to the tissue texture [10]. We use this parameter to tune the tissue SNR to quantitatively match that of the corresponding B-mode image. The specific combination of M and λ values are chosen to both match the B-mode SNR and provide the greatest lesion contrast when there are multiple SNR matches.

III. Results

A. Cyst

Fig. 1 shows a fluid-filled cyst, which is a benign mass. The B-mode image in Fig. 1a presents as hypoechoic with possible acoustic clutter near the top of the mass. When SLSC beamforming is applied ($M = 5$ as shown in Fig. 1b), the borders are better defined than in Fig. 1a and the acoustic clutter from the bottom of the mass is removed. The top of the mass contains unexpected coherence. Despite this unexpected coherence, when an ROI is taken filling the majority of the mass, the contrast is significantly improved when compared to the B-mode ultrasound image.

Similarly, contrast is improved in the R-SLSC image of Fig. 1c, which is displayed with $M = 20$ and $\lambda = 1$. The inclusion of additional lags results in higher resolution, evident when comparing the blurred edges of the mass in Fig. 1b to the more distinct edges of the mass in Fig. 1c. In addition, the tissue texture surrounding the mass is smoothed, resulting in improved contrast compared to the B-mode image. The contrast in the B-mode image is -13.64 dB, the contrast in the SLSC image ($M = 5$) is -21.44 dB, and the contrast in the R-SLSC image is -18.50 dB. We achieved an improvement of 7.8 dB when comparing the B-mode image to the SLSC image at $M = 5$, and an improvement of 4.86 dB when comparing the B-mode image to the R-SLSC image ($M = 20$, $\lambda = 1$). By tuning the sparsity parameter, λ, the SNR of the R-SLSC

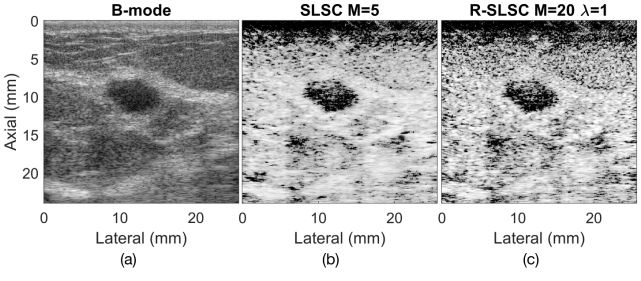

Fig. 1: B-mode (a), SLSC (b), and R-SLSC (c) images of an *in vivo* cyst in a female breast. Images are displayed with 60 dB dynamic range.

image and the speckle SNR of the B-mode image are both 1.6.

B. Fibroadenoma

Fig. 2 shows images of a fibroadenoma in the female breast. Fibroadenomas are benign solid masses that typically present as hypoechoic on ultrasound images [17], [18]. The B-mode image in Fig. 2a shows the mass as hypoechoic. Upon application of SLSC beamforming, Fig. 2b is displayed with short-lag value $M = 5$ and shows a significant amount of coherence within the mass, indicative its solid tissue content. When R-SLSC beamforming is applied and the coherence outliers are removed, (see Fig. 2c which is displayed with $M = 20$ and $\lambda = 1$), the borders of the mass become better distinguished indicating higher resolution than in Fig. 2b due to the inclusion of additional lags.

The contrast of the B-mode image is expected to be better than that of the SLSC image in this case, given the hypoechoic echogenicity of the mass when displaying signal amplitudes in the B-mode image and the "isocoherent" nature of the mass when displaying coherence values in the SLSC images. The contrast for the B-mode, SLSC and R-SLSC images is -14.98 dB, -2.12 dB, and -1.8 dB respectively. Finally, the R-SLSC image parameters are selected to match the B-mode speckle SNR at 1.37.

C. Ductal Carcinoma In Situ

Fig. 3 shows a ductal carcinoma in situ (DCIS) in the *in vivo* female breast, identified at core biopsy. When DCIS presents as a mass, it is typically an ill-dened hypoechoic mass, often with microlobulations and internal echoes [19]. The B-mode image in Fig. 3a follows these typical trends, with distinct but irregular margins of the hypoechoic structure. The SLSC image (shown in Fig. 3b with $M = 5$) similarly has distinct boundaries, but the boundaries are blurred, indicating lower resolution. One option to improve resolution is to include additional lags in the short-lag sum. R-SLSC beamfoming allows these additional lags to be considered with the additional option to tune the sparsity parameter, λ. The R-SLSC image in Fig. 3c is displayed with $M = 20$ and $\lambda = 0.7$, which enables the tissue SNR of the R-SLSC image to match the speckle SNR of the B-mode image. This modification improves resolution due to the additional lags included, demonstrated by the sharper defined edges in Fig. 3c than in Fig. 3b.

The contrast of the B-mode image is -1.97 dB, while the contrast of the SLSC and R-SLSC images is 0.83 dB and 0.75 dB, respectively. The poorer contrast in the SLSC and R-SLSC images when compared to the B-mode image correlates with the solid content of the mass. The solid content is evident as the coherent signal inside of the mass. The SNR of the B-mode, SLSC, and R-SLSC images are 1.32, 1.74, and 1.37, respectively.

D. Duplex Mode Display

Fig. 4 shows an example of a potential clinical overlay method that can be used in conjuction with traditional B-mode imaging to differentiate fluid-filled from solid masses. The R-SLSC images of the masses in Figs. 1 to 3 are overlaid on their corresponding B-mode images. Both the B-mode and the overlaid R-SLSC information are displayed with 60 dB dynamic range, with the B-mode remaining in grayscale and the R-SLSC image displayed on a colormap where red indicates high coherence and blue indicates low coherence.

The differences between solid and fluid-filled masses are evident, where Fig. 4a shows the fluid-filled cyst, which presents as largely blue in the R-SLSC overlay. Figs. 4b and 4c show the fibroadenoma and DCIS, respectively, and are almost completely red, which is indicative of their solid content.

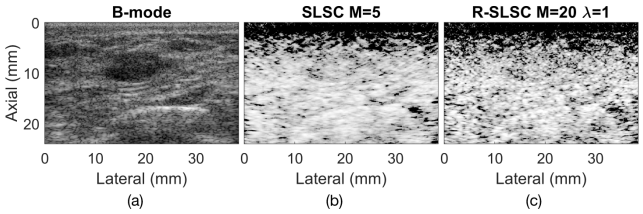

Fig. 2: B-mode (a), SLSC (b), and R-SLSC (c) images of an *in vivo* fibroadenoma in a female breast. Images are displayed with 60 dB dynamic range.

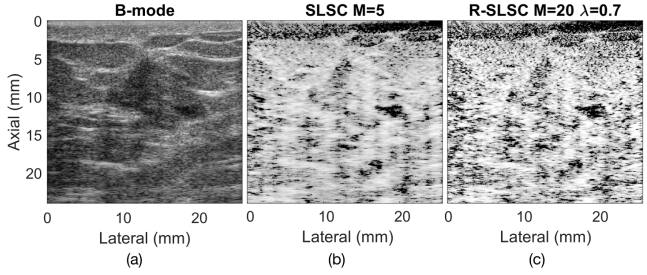

Fig. 3: B-mode (a), SLSC (b), and R-SLSC (c) images of an *in vivo* ductal carcinoma in sito (DCIS) in a female breast. Images are displayed with 60 dB dynamic range.

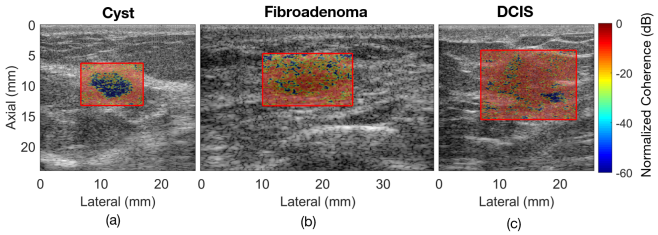

Fig. 4: Example of R-SLSC displayed in duplex mode overlaid on the B-mode image of a cyst (a), fibroadenoma (b), and ductal carcinoma in situ (DCIS) (c). All images, including the overlay are displayed with 60 dB dynamic range.

IV. Discussion

We demonstrated that coherence-based beamforming methods offer improved differentiation between fluid-filled and solid, hypoechoic breast masses based on the coherence information present inside of each mass type. The B-mode images of the cyst, fibroadenoma, and the DCIS shown in Figs. 1a, 2a, and 3a, respectively, are hypoechoic, with similar echogenicity to each other. However, the presence of coherence inside of the R-SLSC image of the two solid masses (i.e., the fibroadenoma, Fig. 2c and the DCIS, Fig. 3c) distinguish them from the fluid-filled cyst of Fig. 1c, which shows minimal coherence. The coherence present at the top of the cyst (i.e., Fig. 1c) is likely due to thicker fluid or debris present inside of the mass, representative of a complicated cyst.

By displaying the coherence information in duplex mode with our proposed approach, as shown in Fig. 4, radiologists can potentially examine the mass using the standard clinical ultrasound imaging workflow, then switch to view the coherence information once a suspicious mass is identified. With this proposed duplex mode, radiologists can first examine tissue features of interest, then engage the added benefits of R-SLSC imaging when needed. These results are promising to extend SLSC and R-SLSC imaging to assist in breast cancer diagnosis. This extension can be particularly beneficial in developing countries where the resources to perform unnecessary biopsies are scarce.

Computational complexity is one disadvantage of R-SLSC, as the technique requires significantly greater processing times than the original SLSC algorithm due to the RPCA step. This computational complexity can be overcome through the block- or patch-wise approach presented in [10].

V. Conclusion

This work is the first to demonstrate the ability of coherence-based imaging methods, specifically SLSC and R-SLSC, to differentiate between solid and fluid-filled hypoechoic breast masses based on the significant difference in contrast and appearance between B-mode and R-SLSC images. Results show promise for using coherence-based beamforming to distinguish solid from fluid hypoechoic breast masses in the clinic. This improvement in distinction can potentially help to lower the false positive rate by allowing for a more definitive diagnosis of benign cysts, reducing the number of biopsy recommendations, and as a result reducing patient stress and discomfort, and saving multiple resources in the healthcare system.

References

[1] F. Bray, J. Ferlay, I. Soerjomataram, R. L. Siegel, L. A. Torre, and A. Jemal, "Global cancer statistics 2018: Globocan estimates of incidence and mortality worldwide for 36 cancers in 185 countries," *CA: A Cancer Journal for Clinicians*, 2018.

[2] W. A. Berg, J. D. Blume, J. B. Cormack, E. B. Mendelson, D. Lehrer, M. Böhm-Vélez, E. D. Pisano, R. A. Jong, W. P. Evans, M. J. Morton *et al.*, "Combined screening with ultrasound and mammography vs mammography alone in women at elevated risk of breast cancer," *Jama*, vol. 299, no. 18, pp. 2151–2163, 2008.

[3] M. T. Mandelson, N. Oestreicher, P. L. Porter, D. White, C. A. Finder, S. H. Taplin, and E. White, "Breast density as a predictor of mammographic detection: Comparison of interval- and screen-detected cancers," *JNCI: Journal of the National Cancer Institute*, vol. 92, no. 13, pp. 1081–1087, 2000.

[4] W. A. Berg, A. I. Bandos, E. B. Mendelson, D. Lehrer, R. A. Jong, and E. D. Pisano, "Ultrasound as the primary screening test for breast cancer: analysis from acrin 6666," *JNCI: Journal of the National Cancer Institute*, vol. 108, no. 4, 2016.

[5] M. A. Lediju, M. J. Pihl, J. J. Dahl, and G. E. Trahey, "Quantitative assessment of the magnitude, impact and spatial extent of ultrasonic clutter," *Ultrasonic Imaging*, vol. 30, no. 3, pp. 151–168, 2008.

[6] M. O'donnell and S. Flax, "Phase aberration measurements in medical ultrasound: human studies," *Ultrasonic Imaging*, vol. 10, no. 1, pp. 1–11, 1988.

[7] R. Entrekin, P. Jackson, J. Jago, and B. Porter, "Real time spatial compound imaging in breast ultrasound: technology and early clinical experience," *medicamundi*, vol. 43, no. 3, pp. 35–43, 1999.

[8] S. Huber, M. Wagner, M. Medl, and H. Czembirek, "Real-time spatial compound imaging in breast ultrasound," *Ultrasound in Medicine & Biology*, vol. 28, no. 2, pp. 155–163, 2002.

[9] M. A. Lediju, G. E. Trahey, B. C. Byram, and J. J. Dahl, "Short-lag spatial coherence of backscattered echoes: Imaging characteristics," *IEEE Transactions on Ultrasonics, Ferroelectrics, and Frequency Control*, vol. 58, no. 7, pp. 1377–1388, 2011.

[10] A. A. Nair, T. D. Tran, and M. A. L. Bell, "Robust short-lag spatial coherence imaging," *IEEE Transactions on Ultrasonics, Ferroelectrics, and Frequency Control*, 2017.

[11] M. A. L. Bell, R. Goswami, J. A. Kisslo, J. J. Dahl, and G. E. Trahey, "Short-lag spatial coherence imaging of cardiac ultrasound data: Initial clinical results," *Ultrasound in Medicine & Biology*, vol. 39, no. 10, pp. 1861–1874, 2013.

[12] V. Kakkad, J. Dahl, S. Ellestad, and G. Trahey, "In vivo application of short-lag spatial coherence and harmonic spatial coherence imaging in fetal ultrasound," *Ultrasonic Imaging*, vol. 37, no. 2, pp. 101–116, 2015.

[13] W. Long, D. Hyun, K. R. Choudhury, D. Bradway, P. McNally, B. Boyd, S. Ellestad, and G. E. Trahey, "Clinical utility of fetal short-lag spatial coherence imaging," *Ultrasound in Medicine & Biology*, 2018.

[14] M. Jakovljevic, G. E. Trahey, R. C. Nelson, and J. J. Dahl, "In vivo application of short-lag spatial coherence imaging in human liver," *Ultrasound in Medicine & Biology*, vol. 39, no. 3, pp. 534–542, 2013.

[15] M. A. L. Bell, J. J. Dahl, and G. E. Trahey, "Resolution and brightness characteristics of short-lag spatial coherence (slsc) images," *IEEE Transactions on Ultrasonics, Ferroelectrics, and Frequency Control*, vol. 62, no. 7, pp. 1265–1276, 2015.

[16] Z. Lin, M. Chen, and Y. Ma, "The augmented lagrange multiplier method for exact recovery of corrupted low-rank matrices," *arXiv preprint arXiv:1009.5055*, 2010.

[17] P. H. Tan and A. A. Sahin, "Fibroepithelial lesions," in *Atlas of differential diagnosis in breast pathology*. Springer, 2017, pp. 51–96.

[18] B. D. Fornage, J. Lorigan, and E. Andry, "Fibroadenoma of the breast: sonographic appearance." *Radiology*, vol. 172, no. 3, pp. 671–675, 1989.

[19] A. Izumori, K. Takebe, and A. Sato, "Ultrasound findings and histological features of ductal carcinoma in situ detected by ultrasound examination alone," *Breast Cancer*, vol. 17, no. 2, pp. 136–141, 2010.